



Article

Structure and Photocatalytic Activity of Copper and Carbon-Doped Metallic Zn Phase-Rich ZnO Oxide Films

Simona Tuckute ¹, Sarunas Varnagiris ¹, Marius Urbonavicius ¹ , Emilija Demikyte ¹ , Kristina Bockute ² and Martynas Lelis ^{1,*}

¹ Center for Hydrogen Energy Technologies, Lithuanian Energy Institute, 3 Breslaujos St., 44403 Kaunas, Lithuania; simona.tuckute@lei.lt (S.T.); sarunas.varnagiris@lei.lt (S.V.); marius.urbonavicius@lei.lt (M.U.); emilija.demikyte@vdu.lt (E.D.)

² Physics Department, Kaunas University of Technology, 50 Studentu St., 51368 Kaunas, Lithuania; kristina.bockute@ktu.lt

* Correspondence: martynas.lelis@lei.lt; Tel.: +370-37-401-904

Abstract: ZnO is one of the most important industrial metal oxide semiconductors. However, in order to fully realise its potential, the electronic structure of ZnO has to be modified to better fit the needs of specific fields. Recent studies demonstrated that reactive magnetron sputtering under Zn-rich conditions promotes the formation of intrinsic ZnO defects and allows the deposition of metallic Zn phase-rich ZnO films. In photocatalytic efficiency tests these films were superior to traditional ZnO oxide, therefore, the purposeful formation of intrinsic ZnO defects, namely Zn interstitials and oxygen vacancies, can be considered as advantageous *self-doping*. Considering that such *self-doped* ZnO remains a semiconductor, the natural question is if it is possible to further improve its properties by adding extrinsic dopants. Accordingly, in the current study, the metallic Zn phase-rich ZnO oxide film formation process (reactive magnetron sputtering) was supplemented by simultaneous sputtering of copper or carbon. Effects of the selected dopants on the structure of *self-doped* ZnO were investigated by X-ray diffractometer, scanning electron microscope, X-ray photoelectron spectroscope and photoluminescence techniques. Meanwhile, its effect on photocatalytic activity was estimated by visible light activated bleaching of Methylene Blue. It was observed that both dopants modify the microstructure of the films, but only carbon has a positive effect on photocatalytic efficiency.

Keywords: photocatalysis; ZnO; zinc oxide; photocatalysts; doping; microstructure; magnetron sputtering



Citation: Tuckute, S.; Varnagiris, S.; Urbonavicius, M.; Demikyte, E.; Bockute, K.; Lelis, M. Structure and Photocatalytic Activity of Copper and Carbon-Doped Metallic Zn Phase-Rich ZnO Oxide Films.

Catalysts **2022**, *12*, 60. <https://doi.org/10.3390/catal12010060>

Academic Editors: Albin Pintar and Gregor Žerjav

Received: 10 December 2021

Accepted: 3 January 2022

Published: 6 January 2022

Publisher's Note: MDPI stays neutral with regard to jurisdictional claims in published maps and institutional affiliations.



Copyright: © 2022 by the authors. Licensee MDPI, Basel, Switzerland. This article is an open access article distributed under the terms and conditions of the Creative Commons Attribution (CC BY) license (<https://creativecommons.org/licenses/by/4.0/>).

1. Introduction

Zinc oxide is an important industrial material extensively used in numerous products such as rubber, plastic, ceramics, glass, medicine, food, pigments, coatings and others [1–5]. In these products, traditional industries exploit the appealing bulk properties of ZnO, namely, high refractive index [6], high thermal stability and conductivity, coupled with a relatively low thermal expansion [5,7], high UV radiation absorbance [8], deodorising and antibacterial properties [9], etc. However, traditional industries use only part of ZnO's potential, because it also has an intriguing set of semiconducting, piezoelectric and pyroelectric properties [10]. Some of these properties are already being applied in commercialised products such as varistors and transparent conducting oxides. However, many more potential applications including nano-electronics, optoelectronics, sensors, field emission, light-emitting diodes, photocatalysis, nanogenerators and nanopiezotronics are still being developed today [10–15].

Naturally, different semiconductor ZnO applications are facing slightly different challenges. However, in general, a lot of them are dealing with the random effects caused by the intrinsic defects which are immanent in zinc oxide [16]. For most semiconductors, traditionally, this would mean the identification, formation and stabilisation of certain electron level configurations which would be the most suitable for the selected applications.

However, for zinc oxide, determination of the credible links between the specific electron energy levels and intrinsic defects (or dopants) that induce them is complicated. For example, it is accepted that the reference band gap value for ZnO is 3.36–3.37 eV [17–19]. In addition, researchers generally agree that oxygen vacancies (V_o), zinc vacancies (V_{Zn}), oxygen interstitials (O_i) and zinc interstitials (Zn_i) are the most common types of intrinsic ZnO defects [20]. However, experimentally observed ZnO band gap values often do not match the reference value and vary from less than 3.2 eV [21] to more than 3.5 eV [22]. Similarly, the review by A. Galdámez-Martínez et al. [23] revealed that positioning of V_{Zn} , O_i , and Zn_i defect levels vary up to 0.5–0.6 eV, while discrepancies in V_o positioning are even wider and exceed 1 eV [18,23,24]. The diversity of these characteristics emphasises the vast possibilities of potential ZnO modifications. However, at the same time, it indicates how strongly distinct ZnO properties depend on the specific synthesis methods and sample history [25].

There are many physical and chemical methods for how to obtain zinc oxide. One of the well-known physical ZnO synthesis methods is the use of a magnetron with a Zn or ZnO target, and its sputtering in an Ar (inert) or Ar + O₂ (reactive) gas atmosphere. Magnetron sputtering has several advantages over traditional wet chemical methods [26]: (i) easy deposition of nearly all metals, alloys and compounds; (ii) high material purity; (iii) strong adhesion with the substrate; (iv) good coverage of curvy surfaces; (v) the possibility of obtaining crystalline phases on heat-sensitive substrates without calcination; and (vi) high uniformity over large surface areas. Moreover, in most cases with magnetron sputtering, it is possible to form coatings with metastable phases whose composition goes beyond the conventional solubility limits [27–29]. Later phenomena are explained by the kinetically limited growth processes that govern thin film structure evolution [30].

Up to now, most of the reported reactive magnetron sputtering ZnO film deposition experiments were performed under relatively oxygen-rich conditions [31–33]. These experiments usually produce highly transparent wurtzite phase ZnO films with strong c-axis oriented growth [34]. On the other hand, it has also been shown that reactive magnetron sputtering under lower partial oxygen pressures can produce nearly opaque dark brown-black ZnO films [35]. These films lose the preference for the c-axis growth and can include a small fraction of the metallic Zn phase. Based on the theoretical modelling, ZnO films produced under Zn-rich conditions stabilise their structure by generating Zn_i and V_o point defects [20]. Zn_i presumably has an energy level positioned approximately 0.22–0.3 eV below the conduction band of ZnO [18,24]. This narrows down the effective band gap of ZnO and enables its photocatalytic response under visible-light irradiation. Indeed, our earlier study demonstrated that reactive magnetron sputtering under Zn-rich conditions promotes the formation of intrinsic ZnO defects and allows the deposition of metallic Zn phase-rich ZnO oxide films. In visible-light photocatalytic efficiency tests these films were superior to traditional ZnO oxide [35], therefore, the purposeful formation of intrinsic ZnO defects, namely Zn interstitials and oxygen vacancies, can be considered advantageous *self-doping*.

Considering that such *self-doped* ZnO remains a semiconductor, the natural question is if it is possible to further improve *self-doped* ZnO properties by adding extrinsic metal or non-metal dopants. For example, it is well known that dopants such as copper [36–39] and carbon [40–42] can reduce the ZnO band gap, lower down the charge recombination rate and enhance its photocatalytic activity. However, how such dopants would affect the properties of self-doped ZnO is not known. Accordingly, in the current work we supplemented the metallic Zn phase-rich ZnO oxide film formation process by simultaneous sputtering of copper or carbon and analysed how these dopants affect the structural and functional properties of *self-doped* ZnO films.

2. Results

2.1. Crystallographic Structure of ZnO Films

The standard molar enthalpy of formation for bulk ZnO is relatively high and reaches -350.5 kJ/mol [43]. This means that if zinc gets in contact with oxygen (especially during reactive magnetron sputtering), it is easily oxidised to ZnO. Zinc oxide can be crystallized in hexagonal wurtzite and cubic zincblende phases. The latter one is less stable and its formation requires specific conditions, therefore during magnetron sputtering ZnO crystallises almost exclusively in the hexagonal structure [44]. Several research groups [31,45] demonstrated that the free surface energies of various wurtzite ZnO planes differ significantly. Naturally, ZnO films produced by reactive magnetron sputtering tend to form the most thermodynamically favourable orientation, which is (002) [31]. The formation enthalpy of ZnO nanoparticles is lower than the formation enthalpy of bulk ZnO [46]. For example, while the formation enthalpy value for bulk ZnO is -350.5 kJ/mol [43], the corresponding values for 50 nm size and 20 nm size nanoparticles are -328.4 kJ/mol and -307.7 kJ/mol, respectively [46]. Accordingly, it is more advantageous thermodynamically to sustain the growth of existing *c*-axis oriented crystals than to form new randomly oriented ZnO nucleates. In practice, this means that by magnetron sputtering scientists usually obtain highly crystalline ZnO films with only one (002) crystallographic orientation.

The described trend can be changed when relatively fast reactive magnetron sputtering is conducted under low partial pressure of oxygen [35,47]. In such cases, zinc does not have enough time to be fully oxidised and the growth of crystalline ZnO regions can be interrupted by random accumulations of oxygen vacancies. Oxygen-depleted domains can become the base points for the formation of new Zn or ZnO nucleates. In scientific reports, these effects reveal themselves as lower film crystallinity, a less pronounced ZnO (002) preferred orientation, or even the appearance of additional hexagonal metallic Zn structures in XRD patterns [35,47,48].

In the current work, we intentionally used a relatively high Ar:O₂ gas flow ratio (5:1) and, without extrinsic dopants, obtained dark opaque metallic Zn phase-rich ZnO films (in the following text denominated as *m*-ZnO). XRD data (Figure 1) confirmed that as-deposited *m*-ZnO film had a polycrystalline structure with nearly all possible orientations of the hexagonal wurtzite ZnO phase (JCPDS card number 01-070-8070). The remaining peaks matched the pattern of the hexagonal metallic Zn phase (JCPDS card number 00-004-0831). Considering the deposition conditions, it would probably be more accurate to name the second phase a solid solution of oxygen in zinc. However, for convenience, in the following text it will be named a (metallic) Zn phase (the optional word *metallic* is added to stress that based on XPS data (provided below) this phase is not considered a zinc suboxide). The crystallite sizes of ZnO and Zn phases in the *m*-ZnO sample were estimated at 9.5 nm and 11.0 nm, respectively. The similarity between the XRD patterns of the *m*-ZnO sample and the most photocatalytically efficient metallic Zn phase rich ZnO oxide film from [35] indicated successful replication of the needed synthesis conditions.

The introduction of Cu additives (in the following text denominated as Cu-ZnO) qualitatively did not change the XRD pattern of the film. However, peak widening reflected crystallite size reduction to 6.7 nm and 3.5 nm for ZnO and metallic Zn phases, respectively. A similar reduction of crystallite size was reported in [36], where the decrease in the crystalline ZnO particle size upon Cu doping was attributed to the formation of Cu–O–Zn bonds, which hinders the growth of crystalline domains.

Lastly, the placement of graphite pieces on the Zn magnetron target (in the following text denominated as *C*-ZnO) resulted in the formation of a higher crystallinity ZnO phase (crystallite size 32.7 nm) with one dominating (002) crystallographic orientation. We assume that partial covering of the Zn target by carbon reduced the rate of zinc sputtering from the target (likewise its condensation at the substrate) and this provided more favourable conditions for the full oxidation of zinc. Consequently, the crystal structure of the ZnO phase was more similar to the transparent ZnO films prepared under conventional oxygen-rich conditions [35,47].

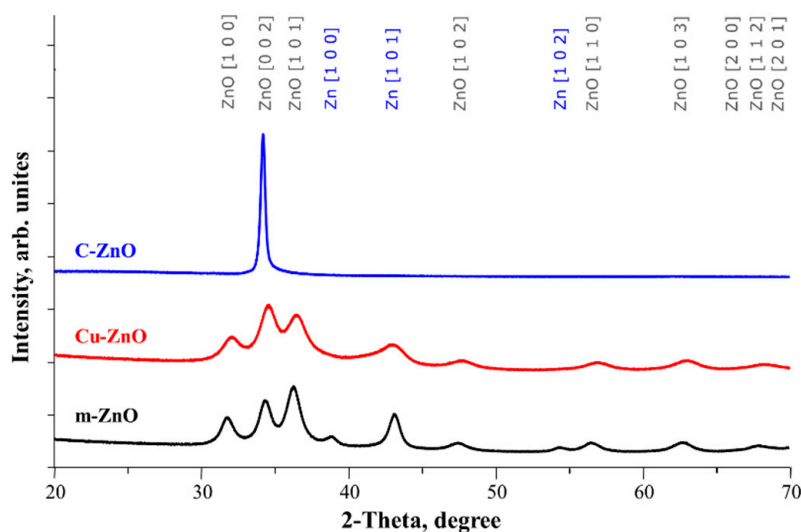


Figure 1. XRD patterns of ZnO films without and with extrinsic dopants: m-ZnO marks ZnO film without extrinsic dopants; Cu-ZnO marks ZnO film doped by copper; C-ZnO film marks ZnO doped by carbon. XRD data recorded using theta–theta modification, Cu K α radiation, Lynx Eye linear position sensitive detector and 0.01° measurement step size.

2.2. Elemental and Chemical Composition of the Films

After deposition, samples were handled in air. Therefore, their surface was covered by adventitious hydrocarbons and adsorbed moisture. In order to determine their nominal elemental composition, samples were alternately sputtered by 2 kV Ar⁺ ions and measured by XPS (Figure 2). The steady concentration value of zinc in the alternately sputtered m-ZnO sample (Figure 2a) was approximately 61–62 at.%. The remaining part was composed entirely of oxygen.

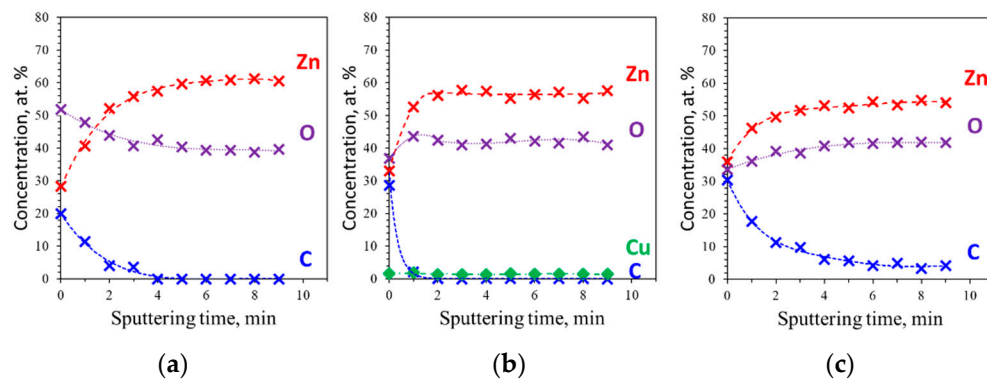


Figure 2. Elemental composition depth profiles of ZnO films (obtained by XPS): (a) m-ZnO; (b) Cu-ZnO; (c) C-ZnO films. Depth profiles were obtained performing alternating photoelectron acquisition and sputtering by 2 kV Ar⁺ ions which were rastered over 2 × 2 mm area.

Different authors [36,37,49] have tested diverse ranges of Cu dopant concentrations and concluded that, up to a certain degree, increasing Cu doping steadily provides higher photocatalytic activity. However, just over the optimal point, the photocatalytic activity of Cu-doped ZnO falls sharply. ZnO co-sputtering using the second magnetron with a Cu target allowed doping the film with approximately 1.5 at.% of Cu (Figure 2b). Such a doping concentration makes up one third of the maximum 5 at.% solubility limit of Cu in ZnO [36] and corresponds well to the optimal Cu concentration values reported in [36] and [49].

Partial Zn target covering by graphite (C-ZnO sample) allowed doping the film with approximately 4 at.% of carbon (Figure 2c). This value was considered appropriate because,

as Bechambi et al. [50] demonstrated, the addition of 4% of carbon still favours the photocatalytic activity of ZnO, whereas a further increase of C doping can decrease the efficiency of the photocatalyst. Such a carbon effect was explained by attributing it to the eventual creation of recombination centres for the photoinduced electron–hole pairs [40].

In addition to providing information about Cu (1.5 at.%) and C (4 at.%) dopant concentrations, elemental depth profiles also revealed a higher than expected reduction of Zn concentrations (in favour of oxygen), which was approximately 5–6 at.% for the copper-doped ZnO and almost 8 at.% for the carbon-doped ZnO. Zinc concentration reduction was considerably larger, than the corresponding amounts of added dopants and this can be seen as the indication of the changed chemical state of Zn. To verify this assumption, we acquired Zn 2p, Zn LMM (Auger electrons) and O 1s spectra (Figure 3). It is known that the Zn 2p electron binding energy difference for ZnO and metallic Zn phases is small (Zn 2p_{3/2} peaks for both compounds usually are positioned in the narrow range between 1021.8–1022.0 eV [51]). Naturally, Zn 2p peaks for all three samples were nearly identical. Meanwhile, Zn LMM Auger electrons are more sensitive to the chemical state of zinc and their spectra showed the expected difference between the samples. Namely, higher kinetic energy peaks (at approximately 992 eV and 995.5 eV) showed the existence of metallic Zn in m-ZnO and Cu-ZnO samples and confirmed the interpretation of the crystallographic data which were presented above (Figure 1).

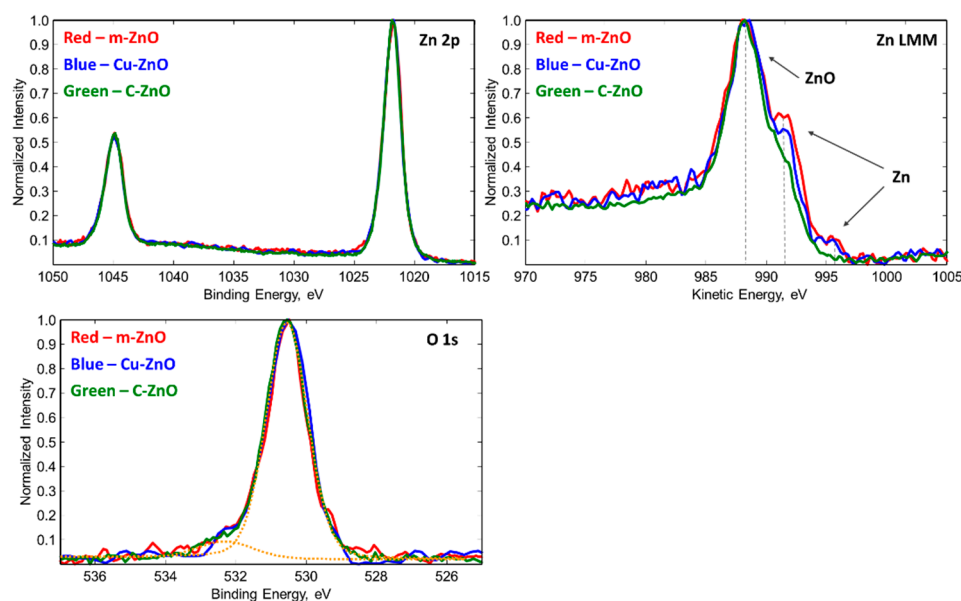


Figure 3. Comparison of Zn 2p, Zn LMM and O 1s electron spectra for m-ZnO (red curve), Cu-ZnO (blue curve), and C-ZnO (green curve) samples. Dotted orange lines in O1s spectra represents the fitting result for the C-ZnO sample, but nearly identical fit was obtained for all free samples. During XPS spectra acquisition (4.5 W, 20 μm focused beam size, 23.5 eV pass energy, 0.2 eV increment), charge neutralisation was realised by a dual neutralisation system consisting of low energy electron and ion beams. Adventitious carbon C 1s peak position of 284.8 eV was used as a neutral charge reference point.

While Zn LMM Auger electrons allowed confirmation of the co-existence of oxidised and non-oxidised zinc phases, O 1s electrons can be used for the estimation of the uniformity of the zinc oxide phase. For instance, some researchers have used O 1s spectra for the identification of oxygen within the stoichiometric hexagonal wurtzite structure (reported peak positions from 529.7 eV up to 530.0 eV) and within the oxygen-deficient regions of the ZnO matrix (reported peak positions from 530.5 eV up to 531.0 eV) [52–54]. In the current work, O 1s spectra for all samples were fitted by two symmetrical peaks located at approximately 530.5–530.6 eV and 532.1–532.3 eV (estimated FWHM values were 1.4 ± 0.05 eV and 1.7 ± 0.1 eV, respectively). Higher binding energy peaks were

attributed to the effect of dopants and the adsorption of moisture/carbon oxide during sample handling in air [52–54]. Meanwhile, lower binding energy peaks were attributed to the Zn–O bond. The symmetry of the strongest peaks and their energy divergence from the stoichiometric ZnO value allow the assumption that all samples had a ZnO phase with relatively high yet similar concentrations of uniformly distributed oxygen vacancies. On the other hand, the noticed differences in elemental composition changes (Figure 2) and Zn LMM Auger electron spectra (Figure 3) suggest that m-ZnO had metallic Zn zones with a relatively very low amount of oxygen impurities. Accordingly, in the XRD pattern of m-ZnO sample (Figure 1) these metallic zinc zones were observed as a separate zinc phase. In the Cu-ZnO sample the share of non-oxidised zinc is reduced (witnessed as reduction of Zn phase crystallite size and lowered intensity of corresponding Auger electron peaks), meanwhile in the C-ZnO sample it is practically not observed. Such a presence and diminishing of the metallic Zn phase explains the higher than expected reduction of zinc concentration in Cu-ZnO and C-ZnO samples.

2.3. Microstructure of Doped and Un-Doped ZnO Films

SEM surface images (Figure 4) revealed, that both m-ZnO and Cu-ZnO films had grainy surfaces with visible feature size below 100 nm, while the average particle size in the granular C-ZnO surface was approximately 200 nm. Similarly, cross-section views showed that m-ZnO sample had a relatively uniform microstructure consisting of randomly distributed fine grains (Figure 4a), whereas C-ZnO film had nearly full-height columns going from the substrate to the surface of the film (Figure 4c). The microstructure of the Cu-ZnO film (Figure 4b) was similar to the m-ZnO sample, however some fine rudiments of the columnar structure (i.e., very fine vertically oriented wrinkles) were already visible throughout the film. Looking at previously reported ZnO microstructures it can be noted that the surface morphology and microstructure of m-ZnO and Cu-ZnO films were relatively similar to the metallic Zn phase rich ZnO oxide films reported in [35]. Meanwhile, SEM images of C-ZnO sample resembled fully oxidised ZnO films from references [35,55,56].

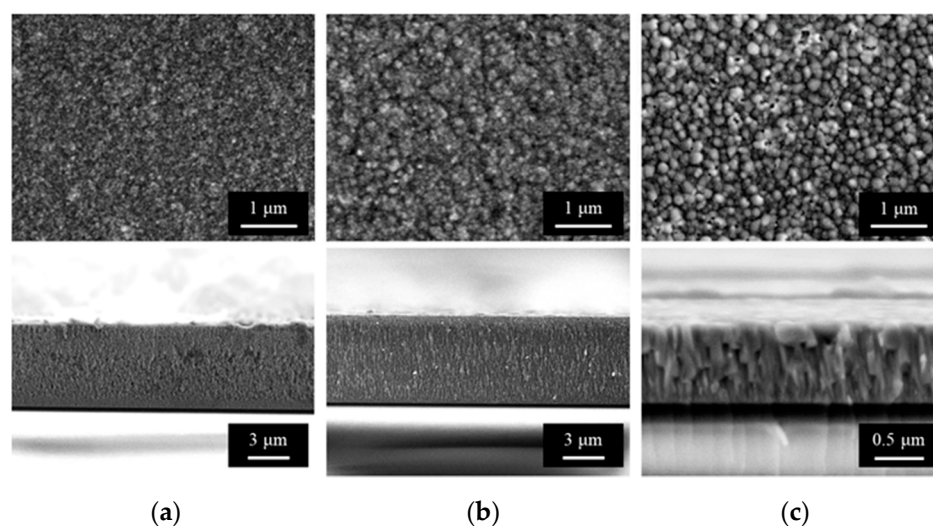


Figure 4. SEM surface (top row) and cross-section (bottom row) images of ZnO films: (a) m-ZnO; (b) Cu-ZnO; (c) C-ZnO. Secondary electron images were obtained using 5 kV electron acceleration voltage.

Another big difference which is visible in the cross-section views is the change in film thickness: 6.2 μm for m-ZnO, 6.3 μm for Cu-ZnO, and approximately 0.95 μm for C-ZnO. Deposition time and magnetron sputtering power for all films were the same (more details on deposition conditions are provided in Section 4.1). Therefore, the smaller thickness of the C-ZnO sample neatly supplements the observations by XRD and XPS. More specifically, the thinner C-ZnO sample supports the idea that carbon pieces reduce the overall sputtering

rate of zinc from the target. This in turn leads to the smaller oxygen consumption by the sputtered zinc and indirectly shifts the reactive magnetron sputtering process from oxygen-deficient to oxygen-rich mode. Accordingly, the Zn LMM Auger electron spectrum of the C-ZnO sample almost does not have a metallic Zn component and its XRD pattern looks similar to the ZnO films which were deposited using relatively high partial pressures of oxygen.

2.4. Photocatalytic Activity of the Films

The photocatalytic methylene blue (MB) bleaching test results are presented in Figure 5. The first order reaction rate constant value for the Cu-ZnO samples ($k = -0.0027 \text{ min}^{-1}$) was slightly higher than for m-ZnO ($k = -0.0024 \text{ min}^{-1}$). This represents little improvement in photocatalytic activity over m-ZnO, whereas the photocatalytic bleaching efficiency with C-ZnO sample was almost 70% higher ($k = -0.0040 \text{ min}^{-1}$) than for the m-ZnO.

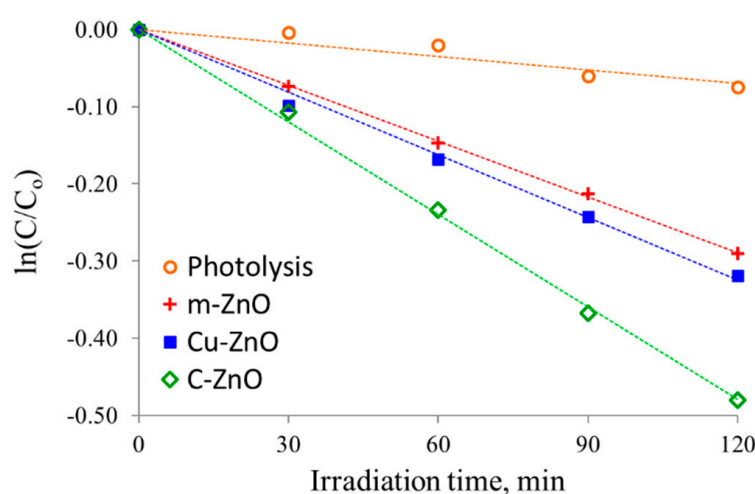


Figure 5. Efficiency of photocatalytic bleaching of aqueous MB solution under visible light irradiation using different photocatalyst films. The tests were performed in a high wall petri dish (40 mm diameter, borosilicate glass) with 7.5 mL of MB solution (initial concentration 10 mg/L). The intensity of the visible light irradiation at MB solution surface was approximately 40 mW/cm^2 .

Previously, a strong positive effect of Cu doping for pristine ZnO was reported by various groups. For example, R.Mohan et al. [38] produced Cu-doped ZnO nanorods and concluded that Cu doping created surface defects which served as favourable traps for the electrons and holes, reduced charge recombination and consequently increased the photocatalytic activity of the rods by approximately a factor of 2. Other researchers [36,37,39] acknowledged the importance of charge separation in Cu-doped ZnO, but they also referred to the significance of the increased concentration of oxygen vacancies and polar surface groups. As was discussed above, metallic Zn phase rich ZnO oxide (i.e., m-ZnO) itself potentially had a significant amount of structural defects and oxygen vacancies. According to the ZnO electron energy diagram compiled by Vempati et al. [18], oxygen vacancies should provide photoluminescence peaks at approximately 500 nm, whereas ZnO surface defects usually result in additional peaks at approximately 450 and 480 nm. For m-ZnO all these peaks can be spotted in its photoluminescence spectrum (Figure 6) and supported the insights from XRD and XPS data. However, it should be noted that in general m-ZnO response to excitation was very weak. This potentially signals that m-ZnO sample has a relatively low electron–hole recombination rate which could be attributed to the presence of the metallic zinc phase. Altogether, it seems that *self-doped* m-ZnO already has most of the enhancements (namely, oxygen vacancies and ZnO surface defects) which were earlier attributed to the copper doping [36,37,39]. Therefore, additional doping of metallic Zn phase-rich ZnO oxide by Cu provided only limited improvement in its photocatalytic performance.

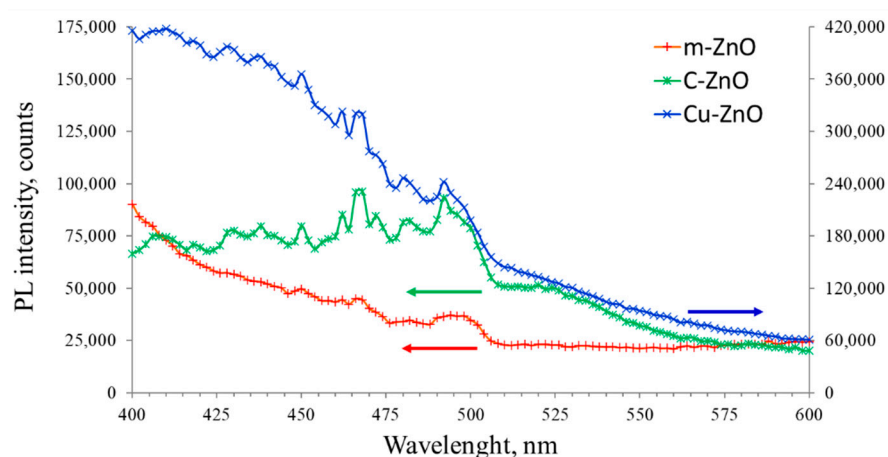


Figure 6. Photoluminescence of m-ZnO, Cu-ZnO and C-ZnO samples. PL spectroscopy measurements were performed using 340 nm excitation source. Arrows indicate intensity scales of the corresponding PL spectra.

Up to now, carbon doping of pristine ZnO studies [40,41] showed that, for photocatalytic applications, ZnO doping by carbon has a strong positive effect which surpasses the effects by other non-metal dopants such as nitrogen and sulphur. Similarly to Cu-doping, carbon doping is acknowledged for its role in the reduction of the recombination rate of photogenerated electron–hole pairs [41,42]. In addition, carbon doping also is known for lowering of ZnO band gap and increasing efficiency in the visible light spectrum [40]. This is achieved by two major effects: first, C-doping increases the Fermi level electron density; second, C-doping introduces a number of new vacant (impurity) states into the band gap, mainly due to the nature of p-type doping [41]. Indeed, the PL spectrum of the C-ZnO sample (Figure 6) has stronger expressed peaks than the m-ZnO and Cu-ZnO samples. Moreover, analysis by Sarkar et al. [57] demonstrated that carbon substituted cationic sites along with the segregation of carbon atoms at the grain boundary regions. All these carbon-induced energy levels and carbon localisation in the grain boundaries of the ZnO structure do not coincide with the effects caused by ZnO *self-doping*. Therefore, in contrast to Cu-doping, we observe that carbon doping significantly strengthened the photocatalytic activity of the C-ZnO sample.

3. Discussions

In a recent article, Wang et al. [58] reviewed advancements in synthesis, properties and applications of various ZnO nanomaterials with oxygen vacancies. It was indicated that oxygen deficient ZnO can be synthesised by various methods including ball milling [59,60], chemical reduction [61–64] and other synthesis or post-treatment procedures under oxygen-deficient conditions [65–70]. Radio frequency (RF) reactive magnetron sputtering [58] was also tried for this purpose, but, in comparison to other methods, its usage was less common (seemingly due to more limited availability than chemical methods, and some process control challenges).

In our previous study we demonstrated that the process of RF reactive magnetron sputtering of Zn in an Ar-O₂ atmosphere has a tendency to shift towards one of two distinct modes: (i) ZnO oxide phase deposition mode, or (ii) metallic Zn phase deposition mode [35]. By using an unconventional gas phase control method (the details are provided in [35]) we managed to stabilise the reactive magnetron sputtering process in between these two modes and deposited metallic Zn phase-rich ZnO oxide films. These films were opaque, had a dark brown-black shade, and their photocatalytic activity was up to 2–3 times higher than conventional ZnO films, which are obtainable using oxygen rich reactive magnetron sputtering. Preliminary analysis of metallic Zn phase-rich ZnO oxide films [35] indicated that these films retained semiconductor properties and had a lot of structural defects

that could be considered as beneficial intrinsic *self-doping* [58]. On the other hand, to our knowledge, the purposeful extrinsic doping of such metallic Zn phase-rich ZnO oxide films was not yet realised and its potential was not yet discussed in the literature.

Accordingly, in the current study, the corresponding reactive zinc magnetron sputtering setup [35] was supplemented by simultaneous sputtering of copper and carbon. The effects of these extrinsic dopants on the structure of ZnO films were investigated by XRD, SEM, XPS and photoluminescence techniques. Meanwhile, its effect on the photocatalytic activity of the films was estimated by the visible-light activated bleaching of methylene blue.

XRD analysis revealed that both m-ZnO and Cu-ZnO samples had a polycrystalline structure with two hexagonal nanocrystalline phases, namely wurtzite ZnO and metallic Zn. Generally, the same phases were observed by XPS analysis as well. Quantitative analysis of XRD and XPS data showed that doping by copper slightly decreased the crystallite size of ZnO and Zn phases. At the same time, it was shown that the addition of copper reduced zinc concentration and lessened the formation of the metallic Zn phase. On the other hand, the placement of carbon pieces on the ZnO target was found to lead to a reduced rate of zinc sputtering. This in turn resulted in smaller oxygen consumption by the sputtered zinc and indirectly shifted the reactive magnetron sputtering process from oxygen-deficient to oxygen-rich mode. Reactive magnetron sputtering deposition under such conditions produced zinc oxide films whose crystallographic structure as well as microstructure were similar to the ZnO films produced under high partial pressures of oxygen [31,45], although oxygen concentration in the film was approximately 40% and the chemical state of zinc (i.e., zinc neighbourhood of Zn in the ZnO phase) was nearly the same for the oxygen deficient ZnO [58].

The photocatalytic bleaching test indicated that the positive effect on photocatalyst efficiency by copper doping was not large, whereas carbon doping increased the efficiency by approximately 70%. The small effect of copper doping was explained by the relatively similar effects caused by the intrinsic ZnO defects (mostly Zn interstitials and oxygen vacancies) and copper dopants. Meanwhile, the reported effect of carbon doping is slightly different [41,42]: (i) it increases the Fermi level electron density; and (ii) introduces a number of new vacant (impurity) states into the band gap. These effects do not concur with the effects caused by the implied intrinsic ZnO defects, therefore carbon doping of highly deficient ZnO films allows for a higher efficiency in visible light photocatalytic bleaching tests. Considering the photocatalytic efficiency difference between the m-ZnO and pristine ZnO samples [35], the overall performance improvement of C-ZnO over conventional ZnO films can be as high, a factor of 3–5.

4. Materials and Methods

4.1. Deposition of the Films

Within this study, three modifications of a physical vapour deposition system (PVD-75, Kurt J. Lesker Company, Jefferson Hills, PA, USA) were used. First, metallic Zn phase-rich ZnO oxide (in the following text denominated as m-ZnO) films were deposited by reactive magnetron sputtering (Figure 7a). For this process one unbalanced magnetron was equipped with a metallic Zn target (76 mm diameter, 99.99% purity) and was powered up for 1 h by an RF power source operating at 150 W. The Ar and O₂ supply ratio (5:1) and total vacuum pressure (1×10^{-2} mbar) were set to match the synthesis conditions of the most photocatalytically efficient sample from our earlier study [35]. Second, to realise metallic Zn phase-rich ZnO oxide doping by carbon, we adopted the method described in [71] and, prior to the sputtering, placed four graphite pieces (approximate size— $10 \times 10 \times 10$ mm) on top of the Zn target (Figure 7b). C-ZnO deposition time, magnetron power, gas phase management and other process parameters were the same as during m-ZnO deposition. Third, to obtain metallic Zn phase-rich ZnO oxide doping by copper, we used an additional unbalanced magnetron (Figure 7c) with metallic Cu target (76 mm diameter, 99.99 purity)

which was powered by a pulsed-DC power supply operating at 80 W (approximately 0.25 A and 320 V). Other process parameters were the same as for m-ZnO and C-ZnO deposition.

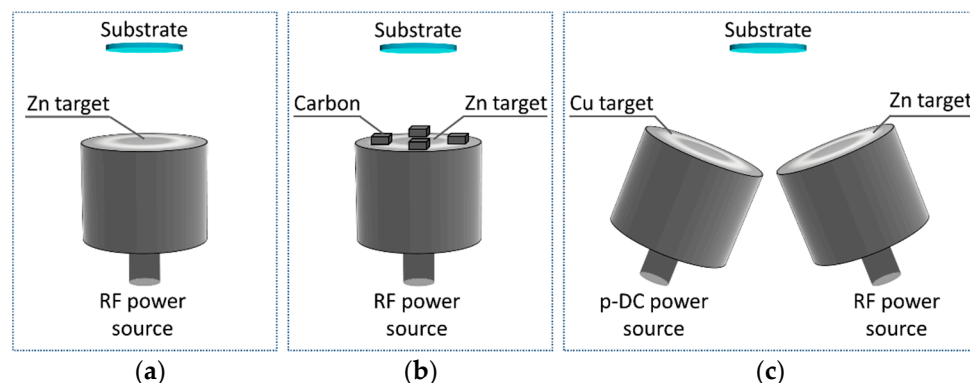


Figure 7. Experimental schemes for the deposition of three types of ZnO based films: (a) metallic Zn phase rich ZnO oxide (m-ZnO); (b) carbon-doped ZnO (C-ZnO); and (c) copper-doped ZnO (Cu-ZnO).

4.2. Structural Analysis

Crystal structure of the films was analysed by a Bruker D8 diffractometer (XRD, Bruker D8, Hamburg, Germany) using a Cu K α radiation and Lynx Eye linear position sensitive detector. The goniometer was working in theta–theta modification, 2 theta scanning range was 20–70°, and the measurement step size was 0.01°. Surface morphology of the films was characterised by Scanning Electron Microscope (SEM, Hitachi S-3400N, Tokyo, Japan). Chemical composition of the samples and elemental distribution depth profiles were measured by X-ray Photoelectron Spectrometer (XPS, PHI 5000 Versaprobe, Boston, MA, USA). Depth profiles were obtained performing alternating sputtering by 2 kV Ar⁺ ions which were rastered over a 2 × 2 mm area. During XPS spectra acquisition, charge neutralisation was realised by dual neutralisation system consisting of low energy electron and ion beams. Adventitious carbon C 1s peak position of 284.8 eV was used as a neutral charge reference point. Photoluminescence (PL) spectroscopy measurements were performed using Edinburgh Instruments FLS980 instrument (Kirkton Campus, United Kingdom) with 340 nm excitation source.

4.3. Photocatalytic Efficiency Estimation

The photocatalytic activity of the films was estimated by adapting the aqueous methylene blue (MB) solution bleaching test procedures that are described in ISO 10678:2010 standard [72]. Before the test, samples were placed into a high wall petri dish (40 mm diameter, borosilicate glass) with 7.5 mL of MB solution (10 mg/L) and kept in the dark for 20–24 h. A SOLIS-3C (5700 K, Thorlabs, Dachau, Germany) visible light LED source was used for the activation of zinc oxide films. The intensity of visible light irradiation at MB solution surface was approximately 40 mW/cm². To minimise the evaporation of the MB solution, the petri dish was covered by a fused silica disk (approximately 90% transmission in whole visible light spectra). All tests were performed using the same freshly prepared MB solution at 23 °C. The efficiency of MB bleaching was measured by UV–VIS spectrophotometer (Jasco V-650, Tokyo, Japan) with regular sample collection (1 mL volume) at 30 min intervals. Immediately after the transmission measurement (i.e., after approximately 1 min), MB solution from the test cuvette was syringed back to the petri-dish with the sample.

5. Conclusions

Recent studies demonstrated that reactive magnetron sputtering under Zn-rich conditions promotes the formation of intrinsic ZnO defects and allows the deposition of metallic Zn phase-rich ZnO films. In photocatalytic efficiency tests these films were superior to traditional ZnO oxide, therefore, the purposeful formation of intrinsic ZnO defects, namely

Zn interstitials and oxygen vacancies, can be considered as advantageous *self-doping*. Considering that such *self-doped* ZnO remains a semiconductor, the natural question was if it is possible to further improve its properties by adding extrinsic dopants. Accordingly, in the current study, the metallic Zn phase-rich ZnO oxide film formation process (reactive magnetron sputtering) was supplemented by simultaneous sputtering of copper or carbon dopant. Effects of the selected dopants on the structure of self-doped ZnO were investigated by X-ray diffractometer, scanning electron microscope, X-ray photoelectron spectroscopy and photoluminescence techniques. Meanwhile, its effect on photo-catalytic activity was estimated by visible light activated bleaching of Methylene Blue. It was observed that both dopants modify the microstructure of the films, but only carbon has a positive effect on their photocatalytic efficiency. The small effect of copper doping was explained by the relatively similar effects caused by the intrinsic ZnO defects (mostly Zn interstitials and oxygen vacancies) and copper dopants.

Author Contributions: Conceptualization and methodology, M.L., S.V. and M.U.; investigation, S.T., S.V., M.U., K.B. and E.D.; writing—original draft preparation, M.L. and S.T.; writing—review and editing, M.L., S.V. and M.U.; visualization, S.T. and M.L. All authors have read and agreed to the published version of the manuscript.

Funding: This research is funded by the European Social Fund according to the activity “Improvement of researchers” qualification by implementing world-class R&D projects of Measure No. 09.3.3-LMT-K-712, project “Investigation of the application of TiO₂ and ZnO for the visible light assisted photocatalytic disinfection of biologically contaminated water” (09.3.3-LMT-K-712-01-0175).

Data Availability Statement: Not applicable.

Acknowledgments: The authors express gratitude for Giedrius Laukaitis for his valuable input in conceptualization and interpretation of experimental results; Mindaugas Aikas and Rolandas Uscila for their input in preparation of the samples and testing facilities.

Conflicts of Interest: The authors declare no conflict of interest.

References

1. Mazitova, A.K.; Vikhareva, I.N.; Aminova, G.K.; Savicheva, J.N. Application of Zinc Oxide to Obtain and Modify Properties of Adipate Plasticizer of Polyvinyl Chloride. *Polymers* **2020**, *12*, 1728. [[CrossRef](#)]
2. Ahn, C.-W.; Song, H.-C.; Nahm, S.; Priya, S.; Park, S.-H.; Uchino, K.; Lee, H.-G.; Lee, H.-J. Effect of ZnO and CuO on the Sintering Temperature and Piezoelectric Properties of a Hard Piezoelectric Ceramic. *J. Am. Ceram. Soc.* **2006**, *89*, 921–925. [[CrossRef](#)]
3. Akintelu, S.A.; Folorunso, A.S. A Review on Green Synthesis of Zinc Oxide Nanoparticles Using Plant Extracts and Its Biomedical Applications. *Bionanoscience* **2020**, *10*, 848–863. [[CrossRef](#)]
4. El Fawal, G.; Hong, H.; Song, X.; Wu, J.; Sun, M.; He, C.; Mo, X.; Jiang, Y.; Wang, H. Fabrication of antimicrobial films based on hydroxyethylcellulose and ZnO for food packaging application. *Food Packag. Shelf Life* **2020**, *23*, 100462. [[CrossRef](#)]
5. Mu, Q.; Feng, S.; Diao, G. Thermal conductivity of silicone rubber filled with ZnO. *Polym. Compos.* **2007**, *28*, 125–130. [[CrossRef](#)]
6. Yoshikawa, H.; Adachi, S. Optical Constants of ZnO. *Jpn. J. Appl. Phys.* **1997**, *36*, 6237–6243. [[CrossRef](#)]
7. Ellmer, K.; Klein, A. ZnO and Its Applications BT. In *Transparent Conductive Zinc Oxide: Basics and Applications in Thin Film Solar Cells*; Ellmer, K., Klein, A., Rech, B., Eds.; Springer: Berlin, Germany, 2008; pp. 1–33. ISBN 978-3-540-73612-7.
8. Weldegebrieal, G.K. Synthesis method, antibacterial and photocatalytic activity of ZnO nanoparticles for azo dyes in wastewater treatment: A review. *Inorg. Chem. Commun.* **2020**, *120*, 108140. [[CrossRef](#)]
9. Padmavathy, N.; Vijayaraghavan, R. Enhanced bioactivity of ZnO nanoparticles-an antimicrobial study. *Sci. Technol. Adv. Mater.* **2008**, *9*, 35004. [[CrossRef](#)] [[PubMed](#)]
10. Wang, Z.L. Ten years’ venturing in ZnO nanostructures: From discovery to scientific understanding and to technology applications. *Chin. Sci. Bull.* **2009**, *54*, 4021. [[CrossRef](#)]
11. Le, A.T.; Ahmadipour, M.; Pung, S.-Y. A review on ZnO-based piezoelectric nanogenerators: Synthesis, characterization techniques, performance enhancement and applications. *J. Alloy. Compd.* **2020**, *844*, 156172. [[CrossRef](#)]
12. Di Mauro, A.; Farrugia, C.; Abela, S.; Refalo, P.; Grech, M.; Falqui, L.; Privitera, V.; Impellizzeri, G. Synthesis of ZnO/PMMA nanocomposite by low-temperature atomic layer deposition for possible photocatalysis applications. *Mater. Sci. Semicond. Processing* **2020**, *118*, 105214. [[CrossRef](#)]
13. Ul Haq, B.; AlFaify, S.; Alshahrani, T.; Ahmed, R.; Butt, F.K.; Ur Rehman, S.; Tariq, Z. Devising square- and hexagonal-shaped monolayers of ZnO for nanoscale electronic and optoelectronic applications. *Sol. Energy* **2020**, *211*, 920–927. [[CrossRef](#)]
14. Faisal, A.D.; Ismail, R.A.; Khalef, W.K.; Salim, E.T. Synthesis of ZnO nanorods on a silicon substrate via hydrothermal route for optoelectronic applications. *Opt. Quantum Electron.* **2020**, *52*, 212. [[CrossRef](#)]

15. Wasim, M.; Shi, F.; Liu, J.; Farooq, A.; Khan, S.U.; Salam, A.; Hassan, T.; Zhao, X. An overview of Zn/ZnO modified cellulosic nanocomposites and their potential applications. *J. Polym. Res.* **2021**, *28*, 338. [[CrossRef](#)]
16. Özgür, Ü.; Alivov, Y.I.; Liu, C.; Teke, A.; Reshchikov, M.A.; Doğan, S.; Avrutin, V.; Cho, S.-J.; Morkoç, H. A comprehensive review of ZnO materials and devices. *J. Appl. Phys.* **2005**, *98*, 041301. [[CrossRef](#)]
17. Lee, C.-T. Fabrication Methods and Luminescent Properties of ZnO Materials for Light-Emitting Diodes. *Materials* **2010**, *3*, 2218–2259. [[CrossRef](#)]
18. Vempati, S.; Mitra, J.; Dawson, P. One-step synthesis of ZnO nanosheets: A blue-white fluorophore. *Nanoscale Res. Lett.* **2012**, *7*, 470. [[CrossRef](#)]
19. Das, D.; Mondal, P. Low temperature grown ZnO:Ga films with predominant c-axis orientation in wurtzite structure demonstrating high conductance, transmittance and photoluminescence. *RSC Adv.* **2016**, *6*, 6144–6153. [[CrossRef](#)]
20. Guan, Y.; Hou, Q.; Xia, D. Effect of intrinsic point defects on ZnO electronic structure and absorption spectra. *Int. J. Mod. Phys.* **2020**, *34*, 2050147. [[CrossRef](#)]
21. Razavi-Khosroshahi, H.; Edalati, K.; Wu, J.; Nakashima, Y.; Arita, M.; Ikoma, Y.; Sadakiyo, M.; Inagaki, Y.; Staykov, A.; Yamauchi, M.; et al. High-pressure zinc oxide phase as visible-light-active photocatalyst with narrow band gap. *J. Mater. Chem.* **2017**, *5*, 20298–20303. [[CrossRef](#)]
22. Shaik, U.P.; Kumar, P.A.; Krishna, M.G.; Rao, S.V. Morphological manipulation of the nonlinear optical response of ZnO thin films grown by thermal evaporation. *Mater. Res. Express* **2014**, *1*, 46201. [[CrossRef](#)]
23. Galdámez-Martínez, A.; Santana, G.; Güell, F.; Martínez-Alanis, P.R.; Dutt, A. Photoluminescence of ZnO Nanowires: A Review. *Nanomaterials* **2020**, *10*, 857. [[CrossRef](#)]
24. Al-Hilli, S.; Willander, M. The pH Response and Sensing Mechanism of n-Type ZnO/Electrolyte Interfaces. *Sensors* **2009**, *9*, 7445–7480. [[CrossRef](#)]
25. Ellmer, K. Magnetron sputtering of transparent conductive zinc oxide: Relation between the sputtering parameters and the electronic properties. *J. Phys. Appl. Phys.* **2000**, *33*, R17–R32. [[CrossRef](#)]
26. Swann, S. Magnetron sputtering. *Phys. Technol.* **1988**, *19*, 67–75. [[CrossRef](#)]
27. Petrov, I.; Barna, P.B.; Hultman, L.; Greene, J.E. Microstructural evolution during film growth. *J. Vac. Sci. Technol.* **2003**, *21*, S117–S128. [[CrossRef](#)]
28. Barna, P.B.; Adamik, M. Fundamental structure forming phenomena of polycrystalline films and the structure zone models. *Thin Solid Film.* **1998**, *317*, 27–33. [[CrossRef](#)]
29. Grovenor, C.R.M.; Hentzell, H.T.G.; Smith, D.A. The development of grain structure during growth of metallic films. *Acta Metall.* **1984**, *32*, 773–781. [[CrossRef](#)]
30. Chang, K.; Music, D.; Baben, M.; Lange, D.; Bolvardi, H.; Schneider, J.M. Modeling of metastable phase formation diagrams for sputtered thin films. *Sci. Technol. Adv. Mater.* **2016**, *17*, 210–219. [[CrossRef](#)] [[PubMed](#)]
31. Kunj, S.; Sreenivas, K. Residual stress and defect content in magnetron sputtered ZnO films grown on unheated glass substrates. *Curr. Appl. Phys.* **2016**, *16*, 748–756. [[CrossRef](#)]
32. Ievtushenko, A.I.; Karpyna, V.A.; Lazorenko, V.I.; Lashkarev, G.V.; Khranovskyy, V.D.; Baturin, V.A.; Karpenko, O.Y.; Lunika, M.M.; Avramenko, K.A.; Strelchuk, V.V.; et al. High quality ZnO films deposited by radio-frequency magnetron sputtering using layer by layer growth method. *Thin Solid Film.* **2010**, *518*, 4529–4532. [[CrossRef](#)]
33. Chen, H.; Ding, J.; Shi, F.; Li, Y.; Guo, W. Optical properties of Ti-doped ZnO films synthesized via magnetron sputtering. *J. Alloy. Compd.* **2012**, *534*, 59–63. [[CrossRef](#)]
34. Mosquera, A.A.; Horwat, D.; Rashkovskiy, A.; Kovalev, A.; Miska, P.; Wainstein, D.; Albella, J.M.; Endrino, J.L. Exciton and core-level electron confinement effects in transparent ZnO thin films. *Sci. Rep.* **2013**, *3*, 1714. [[CrossRef](#)]
35. Lelis, M.; Tuckute, S.; Varnagiris, S.; Urbonavicius, M.; Bockute, K.; Laukaitis, G. Synthesis and analysis of metallic Zn phase rich ZnO oxide films for the photocatalytic water treatment technologies. *Mater. Today Proc.* **2020**, *33*, 2484–2489. [[CrossRef](#)]
36. Fu, M.; Li, Y.; Wu, S.; Lu, P.; Liu, J.; Dong, F. Sol-gel preparation and enhanced photocatalytic performance of Cu-doped ZnO nanoparticles. *Appl. Surf. Sci.* **2011**, *258*, 1587–1591. [[CrossRef](#)]
37. Pawar, R.C.; Choi, D.-H.; Lee, J.-S.; Lee, C.S. Formation of polar surfaces in microstructured ZnO by doping with Cu and applications in photocatalysis using visible light. *Mater. Chem. Phys.* **2015**, *151*, 167–180. [[CrossRef](#)]
38. Mohan, R.; Krishnamoorthy, K.; Kim, S.-J. Enhanced photocatalytic activity of Cu-doped ZnO nanorods. *Solid State Commun.* **2012**, *152*, 375–380. [[CrossRef](#)]
39. Kadam, A.N.; Kim, T.G.; Shin, D.S.; Garadkar, K.M.; Park, J. Morphological evolution of Cu doped ZnO for enhancement of photocatalytic activity. *J. Alloy. Compd.* **2017**, *710*, 102–113. [[CrossRef](#)]
40. Kumari, V.; Mittal, A.; Jindal, J.; Yadav, S.; Kumar, N. S-, N- and C-doped ZnO as semiconductor photocatalysts: A review. *Front. Mater. Sci.* **2019**, *13*, 1–22. [[CrossRef](#)]
41. Yu, W.; Zhang, J.; Peng, T. New insight into the enhanced photocatalytic activity of N-, C- and S-doped ZnO photocatalysts. *Appl. Catal. Environ.* **2016**, *181*, 220–227. [[CrossRef](#)]
42. Ansari, S.A.; Ansari, S.G.; Foad, H.; Cho, M.H. Facile and sustainable synthesis of carbon-doped ZnO nanostructures towards the superior visible light photocatalytic performance. *New J. Chem.* **2017**, *41*, 9314–9320. [[CrossRef](#)]
43. Fan, G.; Huang, Z.; Jiang, J.; Sun, L. Standard molar enthalpy of formation of the ZnO nanosheets. *J. Therm. Anal. Calorim.* **2012**, *110*, 1471–1474. [[CrossRef](#)]

44. Ashrafi, A.; Jagadish, C. Review of zincblende ZnO: Stability of metastable ZnO phases. *J. Appl. Phys.* **2007**, *102*, 071101. [[CrossRef](#)]
45. Al-Hardan, N.H.; Abdullah, M.J.; Abdul Aziz, A.; Ahmad, H.; Rashid, M. The effect of oxygen ratio on the crystallography and optical emission properties of reactive RF sputtered ZnO films. *Phys. Condens. Matter* **2010**, *405*, 1081–1085. [[CrossRef](#)]
46. Hu, S.X.; Li, Y.; Wu, X.M. The Standard Formation Enthalpies of Spherical ZnO Nano-Particles: Size Matters. *Adv. Mater. Res.* **2015**, *1118*, 62–66. [[CrossRef](#)]
47. Masłyk, M.; Borysiewicz, M.A.; Wzorek, M.; Wojciechowski, T.; Kwoka, M.; Kamińska, E. Influence of absolute argon and oxygen flow values at a constant ratio on the growth of Zn/ZnO nanostructures obtained by DC reactive magnetron sputtering. *Appl. Surf. Sci.* **2016**, *389*, 287–293. [[CrossRef](#)]
48. Varnagiris, S.; Urbonavicius, M.; Tuckute, S.; Lelis, M. Formation of Zn-rich ZnO films with improved bulk and surface characteristics by approach of magnetron sputtering technique. *Thin Solid Film.* **2021**, *738*, 138967. [[CrossRef](#)]
49. Vaiano, V.; Iervolino, G.; Rizzo, L. Cu-doped ZnO as efficient photocatalyst for the oxidation of arsenite to arsenate under visible light. *Appl. Catal. Environ.* **2018**, *238*, 471–479. [[CrossRef](#)]
50. Bechambi, O.; Sayadi, S.; Najjar, W. Photocatalytic degradation of bisphenol A in the presence of C-doped ZnO: Effect of operational parameters and photodegradation mechanism. *J. Ind. Eng. Chem.* **2015**, *32*, 201–210. [[CrossRef](#)]
51. NIST X-ray Photoelectron Spectroscopy Database; NIST Standard Reference Database 20; National Institute of Standards and Technology: Gaithersburg, MD, USA, 2000; (updated 2012).
52. Abdel-wahab, M.S.; Jilani, A.; Yahia, I.S.; Al-Ghamdi, A.A. Enhanced the photocatalytic activity of Ni-doped ZnO thin films: Morphological, optical and XPS analysis. *Superlattices Microstruct.* **2016**, *94*, 108–118. [[CrossRef](#)]
53. Guo, H.-L.; Zhu, Q.; Wu, X.-L.; Jiang, Y.-F.; Xie, X.; Xu, A.-W. Oxygen deficient ZnO_{1-x} nanosheets with high visible light photocatalytic activity. *Nanoscale* **2015**, *7*, 7216–7223. [[CrossRef](#)]
54. Al-Gaashani, R.; Radiman, S.; Daud, A.R.; Tabet, N.; Al-Douri, Y. XPS and optical studies of different morphologies of ZnO nanostructures prepared by microwave methods. *Ceram. Int.* **2013**, *39*, 2283–2292. [[CrossRef](#)]
55. Swatowska, B.; Powroźnik, W.; Czternastek, H.; Lewińska, G.; Stapiński, T.; Pietruszka, R.; Witkowski, B.S.; Godlewski, M. Application Properties of ZnO and AZO Thin Films Obtained by the ALD Method. *Energies* **2021**, *14*, 6271. [[CrossRef](#)]
56. Medina-Montes, M.I.; Lee, S.H.; Pérez, M.; Baldenegro-Pérez, L.A.; Quevedo-López, M.A.; Gnade, B.; Ramírez-Bon, R. Effect of Sputtered ZnO Layers on Behavior of Thin-Film Transistors Deposited at Room Temperature in a Nonreactive Atmosphere. *J. Electron. Mater.* **2011**, *40*, 1461–1469. [[CrossRef](#)]
57. Sarkar, D.; Ghosh, C.K.; Chattopadhyay, K.K. Carbon doped ZnO thin film: Unusual nonlinear variation in bandgap and electrical characteristic. *Appl. Surf. Sci.* **2017**, *418*, 252–257. [[CrossRef](#)]
58. Wang, J.; Chen, R.; Xiang, L.; Komarneni, S. Synthesis, properties and applications of ZnO nanomaterials with oxygen vacancies: A review. *Ceram. Int.* **2018**, *44*, 7357–7377. [[CrossRef](#)]
59. Chen, D.; Wang, Z.; Ren, T.; Ding, H.; Yao, W.; Zong, R.; Zhu, Y. Influence of defects on the photocatalytic activity of ZnO. *J. Phys. Chem.* **2014**, *118*, 15300–15307. [[CrossRef](#)]
60. Aggelopoulos, C.A.; Dimitropoulos, M.; Govatsi, A.; Sygellou, L.; Tsakiroglou, C.D.; Yannopoulos, S.N. Influence of the surface-to-bulk defects ratio of ZnO and TiO₂ on their UV-mediated photocatalytic activity. *Appl. Catal. Environ.* **2017**, *205*, 292–301. [[CrossRef](#)]
61. Yao, C.; Wei, B.; Ma, H.; Li, H.; Meng, L.; Zhang, X.; Gong, Q. Enhanced photoelectrochemical performance of hydrogenated ZnO hierarchical nanorod arrays. *J. Power Sources* **2013**, *237*, 295–299. [[CrossRef](#)]
62. Lu, X.; Wang, G.; Xie, S.; Shi, J.; Li, W.; Tong, Y.; Li, Y. Efficient photocatalytic hydrogen evolution over hydrogenated ZnO nanorod arrays. *Chem. Commun.* **2012**, *48*, 7717–7719. [[CrossRef](#)]
63. Wang, C.; Wu, D.; Wang, P.; Ao, Y.; Hou, J.; Qian, J. Effect of oxygen vacancy on enhanced photocatalytic activity of reduced ZnO nanorod arrays. *Appl. Surf. Sci.* **2015**, *325*, 112–116. [[CrossRef](#)]
64. Ansari, S.A.; Khan, M.M.; Kalathil, S.; Nisar, A.; Lee, J.; Cho, M.H. Oxygen vacancy induced band gap narrowing of ZnO nanostructures by an electrochemically active biofilm. *Nanoscale* **2013**, *5*, 9238–9246. [[CrossRef](#)] [[PubMed](#)]
65. Xing, G.; Wang, D.; Yi, J.; Yang, L.; Gao, M.; He, M.; Yang, J.; Ding, J.; Sum, T.C.; Wu, T. Correlated d₀ ferromagnetism and photoluminescence in undoped ZnO nanowires. *Appl. Phys. Lett.* **2010**, *96*, 112511. [[CrossRef](#)]
66. Asok, A.; Gandhi, M.N.; Kulkarni, A.R. Enhanced visible photoluminescence in ZnO quantum dots by promotion of oxygen vacancy formation. *Nanoscale* **2012**, *4*, 4943–4946. [[CrossRef](#)] [[PubMed](#)]
67. Ahn, M.-W.; Park, K.-S.; Heo, J.-H.; Park, J.-G.; Kim, D.-W.; Choi, K.J.; Lee, J.-H.; Hong, S.-H. Gas sensing properties of defect-controlled ZnO-nanowire gas sensor. *Appl. Phys. Lett.* **2008**, *93*, 263103. [[CrossRef](#)]
68. Tian, J.L.; Wang, G.G.; Zhang, H.Y. Effect of Annealing Atmosphere on the Structural and Optical Properties of ZnO Thin Films on Si (100) Substrates Grown by Atomic Layer Deposition. In *Journal of Nano Research*; Trans Tech Publications Ltd.: Freienbach, Switzerland, 2016; Volume 37, pp. 92–98. [[CrossRef](#)]
69. Wang, J.; Wang, Z.; Huang, B.; Ma, Y.; Liu, Y.; Qin, X.; Zhang, X.; Dai, Y. Oxygen Vacancy Induced Band-Gap Narrowing and Enhanced Visible Light Photocatalytic Activity of ZnO. *ACS Appl. Mater. Interfaces* **2012**, *4*, 4024–4030. [[CrossRef](#)]
70. Camarda, P.; Messina, F.; Vaccaro, L.; Agnello, S.; Buscarino, G.; Schneider, R.; Popescu, R.; Gerthsen, D.; Lorenzi, R.; Gelardi, F.M.; et al. Luminescence mechanisms of defective ZnO nanoparticles. *Phys. Chem. Chem. Phys.* **2016**, *18*, 16237–16244. [[CrossRef](#)]

-
71. Varnagiris, S.; Medvids, A.; Lelis, M.; Milcius, D.; Antuzevics, A. Black carbon-doped TiO₂ films: Synthesis, characterization and photocatalysis. *J. Photochem. Photobiol. Chem.* **2019**, *382*, 111941. [[CrossRef](#)]
 72. Fine Ceramics (Advanced Ceramics, Advanced Technical Ceramics). In *Determination of Photocatalytic Activity of Surfaces in an Aqueous Medium by Degradation of Methylene Blue*; ISO: Geneva, Switzerland, 2010; pp. 1–12.